

# CALIBRATION AND CHARACTERIZATION OF CAPACITIVE OST QUENCH DETECTORS FOR SRF CAVITIES AT IPN ORSAY

M. Fouaidy, F. Dubois, J-M. Dufour, D. Longuevergne, G. Michel, A. Maroni, J-F Yaniche, IPN Orsay Unité mixte de recherche CNRS-IN2P3 Université Paris-Sud 91406 ORSAY cedex

## Abstract

The maximum RF surface magnetic field ( $B_S$ ) achieved with SRF bulk Nb cavities is often limited by anomalous losses due to Joule heating of normal-resistive defects embedded onto the RF surface. At high  $B_S$  (e.g.  $B_S > 50$  mT), the defect temperature increases strongly with  $B_S$ , leading to a thermal runaway of the cavity or quench. The unloaded quality factor  $Q_0$  of the cavity decreases suddenly and strongly due to superconducting to normal state phase transition of the hot spot area. Quench detectors, called Oscillating Superleak Transducer (OST) and sensing 2<sup>nd</sup> sound events in He II, have been recently used to study quench of SRF cavities. IPN developed its prototypes of OST quench detectors and a test stand for their calibration and characterization in the temperature range  $T_0 = 1.6$  K-2.2 K. This device allows precise and controlled experimental simulation of SRF cavity quench using pulsed heat sources. Experiments were performed to study the dynamic response of OST detectors when the heat source is subjected to a time varying heat flux  $q(t)$  as function of several parameters ( $T_0$ ,  $q(t)$  time structure and density, heat source size) and first experimental data are presented.

## INTRODUCTION

Thanks to the tremendous R&D effort by different laboratories around the world and to the use of high purity material and well assessed fabrication and preparation procedure, SRF bulk niobium cavities are nowadays operated reliably at high accelerating gradient which correspond to surface magnetic field  $B_S > 50$  mT [1]. However, the maximum RF surface magnetic field ( $B_{Smax}$ ) achieved with SRF bulk Nb cavities is often limited by anomalous RF losses due to Joule heating of normal-resistive defects or inclusions embedded [1-2] onto the RF surface. The typical effective diameter and surface resistance of these defects are respectively in the range 1-100  $\mu\text{m}$  and 1-10 m $\Omega$ . For example at  $B_S = 50$  mT, the heat flux density  $q_{\text{Defect}}$  due to Joule heating of a defect area is  $0.8 \cdot 10^6$  W/m<sup>2</sup> in contrast to RF losses in the superconducting RF surface region ( $q_{\text{SRF}} \sim 0.8$  W/m<sup>2</sup>). Due to such very high heat flux in a defect zone, and to the quadratic dependence of Joule RF losses with  $B_S$  (e.g.  $q \propto R_S B_S^2$ ), the temperature increases strongly with  $B_S$  especially in the defect area. This heating increases the RF surface temperature in the vicinity of the defect beyond the critical temperature  $T_C$  ( $B_S$ ) of niobium resulting in a dramatic increase (e.g. by 5 to 6 orders of magnitude) of the local RF losses. This catastrophic process leads generally to a thermal runaway of the SRF cavity or quench as soon as the hot spot area effective

diameter exceeds a critical value for which the unloaded quality factor  $Q_0$  decreases strongly. Obviously, the thermal quench of SRF cavity is easily detectable with RF probes (i.e. transmitted and/or reflected RF power). However, as it is an overall measurement, RF signals are insufficient to characterize completely the thermal runaway and are unable to locate quench source. Dedicated diagnostic tools are then needed in order to study thoroughly and investigate in details quench phenomena.

## BRIEF HISTORY OF THERMAL DIAGNOSTIC TOOLS OF ANOMALOUS RF LOSSES IN SRF CAVITIES

The first generation of sensors dedicated to diagnostic of anomalous RF losses and thermal breakdown events was developed in  $\sim 1980$ . These sensors are special surface thermometers (Fig. 1), which allow the measurement of the outer surface temperature [3-5] of SRF cavities cooled by Liquid Helium (LHe). These thermometric resistive sensors, which operate in sub-cooled normal LHe or He I bath or saturated superfluid helium bath, are of two types: a) Scanning Surface Thermometers (SST), b) Fixed Surface Thermometers (FST).

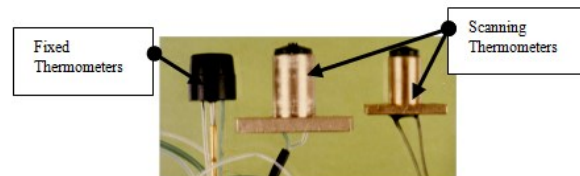


Fig. 1: Surface thermometers of IPN Orsay for measurement of liquid helium cooled SRF cavities wall temperature.

Due to the cooling medium (saturated boiling He I, sub-cooled He I, saturated superfluid helium or He II at bath temperature  $T_{\text{bath}} < T_\lambda$ ) and the measurement configuration, SST are intrinsically limited [3-4] when operated in He II: 1) low measurement efficiency ( $\sim 1-2\%$ ), 2) lack of reliability, lack of repeatability. FST are also practically limited because a large number (i.e.  $\gg 100$ ) of such sensors is needed [4-7] in order to ensure a good spatial resolution. Second generation of quench detectors in superfluid helium, namely OST (Oscillating Super Leak Transducer), were developed in 1970 for fundamental research on He II thermo-hydrodynamics [8]. These OST, which are capacitive quench detectors, based on second sound (temperature wave) measurements in superfluid Helium (He II), were applied to SRF cavity thermal breakdown investigation nearly 5 years ago [9].

More recently, it was suggested to use Low Response Time ( $\ll 1\text{ms}$ ) Resistive Thermometers (LRETIRETH) as quench detectors.

### EXPERIMENTAL SET-UP

#### Description of OST Detectors Developed at IPN Orsay

We used the original design, of OST developed by Z.A Conway [9]. It is a capacitive sensor (Fig. 2-Fig. 3). The first rigid electrode, is a brass disk (O.D: 16 mm, Thickness: 4.1 mm), imbedded in the body of the sensor which is made of aluminium alloy. Moreover, the deformable Active Electrode bonding agent, which is the dielectric insulator is an epoxy resin (STYCAST 2650 MM). The active deformable electrode is a polycarbonate semipermeable (Pore diameter:  $0.2\ \mu\text{m}$ ) membrane of 6 to 11  $\mu\text{m}$  thickness and coated with 50nm thick aluminium onto upper surface for electrical contact. Finally a SMA base connector is attached to the brass electrode.

#### Cryogenic Insert for Calibration and Full

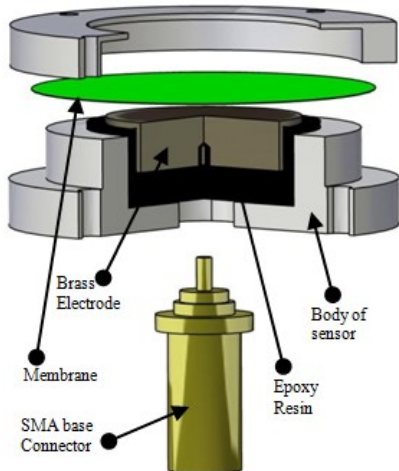


Fig. 2: Main components of OST quench detectors prior to assembling.

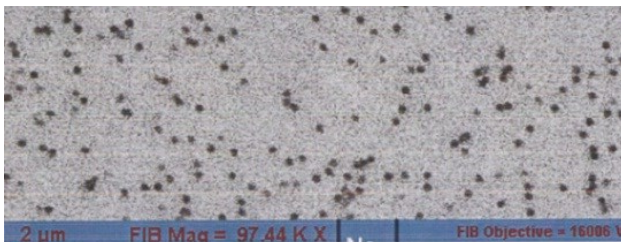


Fig. 3: SEM micrograph of the porous polycarbonate membrane after aluminium coating.

#### Characterization of Quench Detectors

We have developed a new cryogenic insert (Fig. 4) dedicated to the calibration and full characterization of various quench detectors. The main characteristics of the cryostat and insert assembly are: a) Useful height of 1 m, b) Bath temperature range:  $T_{\text{bath}}=1.55\ \text{K}-4.25\ \text{K}$ , c) Static heat load:  $\sim 0.6\ \text{W}-1\ \text{W}$ . The quench of SRF cavities is

experimentally simulated by means of localized resistive heaters creating a precisely controlled pulsed heat flux. A photograph of SMD type resistors used for SRF cavity quench simulation is shown in Fig. 5.

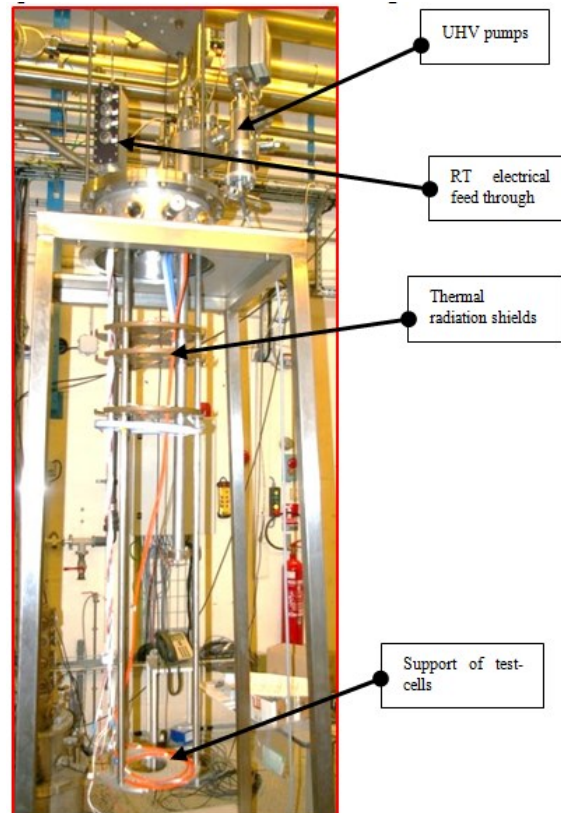


Fig. 4: Cryogenic insert for quench detectors characterization.

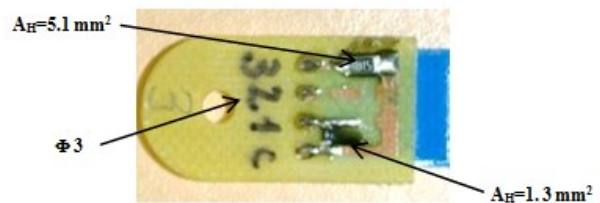


Fig. 5: SMD type resistors.

#### Test Cells and Configuration of Sensors

In order to investigate the effect of the heater geometry, and the distance of the sensors to the quench-like source, we performed experimental runs with different configurations. Cylindrical resistive heaters and SMD resistive heaters of different size were used for this purpose. Moreover, we used two industrial bare ship 1050 BC CERNOX resistors, named CX here after as LRETIRETH. The different experimental configurations tested actually are summarized in Table 1 and a close view of the three test cells used, are illustrated in Fig. 6-Fig. 8. The measured resistances values at  $T_{\text{bath}}=2\ \text{K}$  of the different heaters are in the range  $55\ \Omega - 60\ \Omega$ .

Table 1: Test Cell Configurations

Test cell	Heater geometry	Heater Area (mm <sup>2</sup> )	Sensor type	Sensor location (mm)
1	Cylinder	12.9	CERNOX #1	24.1
		24.2	CERNOX #2	7.7
		79.5		
2	Cylinder	12.9	OST#4	28
		24.2	OST#3	41
		79.5		
3	Flat-SMD	1.3	OST#1	20
		5.1	OST#2	31



Fig. 6: Test cell #1.



Fig. 7: Test cell #2.



Fig. 8: Test cell #3.

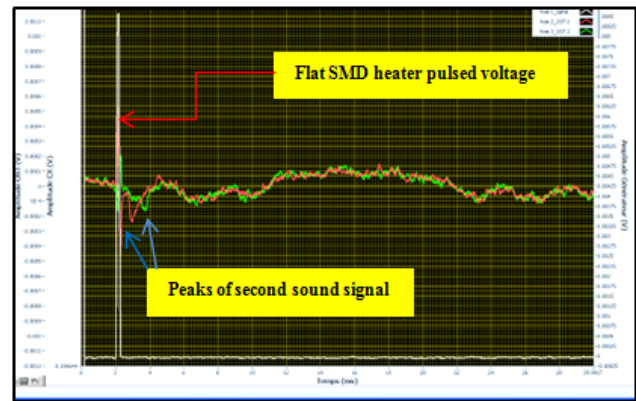
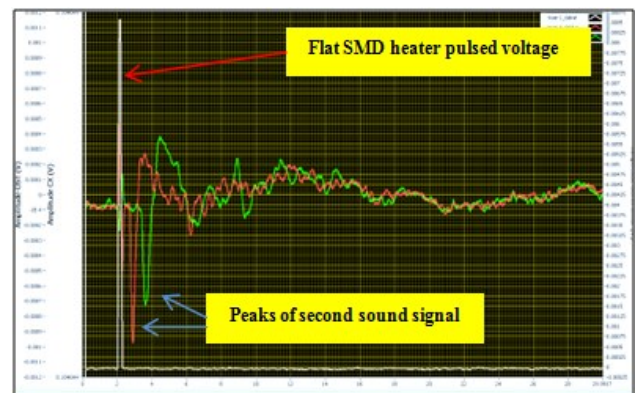
## EXPERIMENTAL RESULTS AND DISCUSSION

### Experimental Procedure

Several experiments were performed at different  $T_{\text{bath}}$ . Prior to the measurements of the response of the sensors (OST and CX), we calibrated the CX resistors by comparison to a CERNOX 1050SD thermometer calibrated at IPN Orsay. For this purpose, we naturally used the Lhe saturated bath as thermostat: using a MKS pressure transducer, a PID pressure controller and a motorized butterfly valve,  $T_{\text{bath}}$  was regulated to better than 0.2 mK for  $T_{\text{bath}} < T_{\lambda} = 2.1768$  K, via the vapour pressure control. After thermometers calibration, we then measured the response of quench detectors to a pulsed heat flux generated by the different heaters.

### The Observed Signals

During the first experimental runs, due to insufficient electromagnetic shielding, we observed very noisy signals for both OST and fast response thermometers. After an important effort of shielding of the whole experimental set-up from the sensors to the data acquisition system, the signal to noise ratio of the thermometric signals was significantly improved (i.e. more than order of magnitude). Two examples of second sound signals as observed at  $T_{\text{bath}} = 2$  K by the sensors OST#1 and OST#2 of the test-cell #3 are illustrated in Fig. 9 Fig. 10 for two different values of the polarization voltage at a given pulsed heat flux (peak value  $q_p = 753$  W/cm<sup>2</sup>) with a pulse duration  $\tau_p = 100$   $\mu$ s and at a repetition rate  $f_{\text{rep}} = 10$  Hz. For the run shown in Fig. 9, the applied polarization DC voltage was  $V_p = 50$  V while in the case depicted in Fig. 10,  $V_p = 150$  V: the measured signal is improved by a factor 5 increasing from 180  $\mu$ V to 890  $\mu$ V when  $V_p$  is increased by a factor 3.

Fig. 9: Response signals of OST #1 (red) and OST #2 (green) to a pulsed heat flux  $q_p = 753$  W/cm<sup>2</sup> for  $V_p = 50$  V.Fig. 10: Response signals of OST#1 (red) and OST#2 (green) to a pulsed heat flux  $q_p = 753$  W/cm<sup>2</sup> for  $V_p = 150$  V.

Notice that two type of behaviour were observed concerning the effect of  $V_p$  on OST signals: a) linear increase of signal amplitude with  $V_p$ , b) amplitude which is not dependent on  $V_p$ . An example of second sound signals as observed at  $T_{\text{bath}} = 2.1$  K by the thermometers CX#1 and CX#2 is shown in Fig. 11 for a pulsed heat

flux (peak heater power  $Q_p = 38$  W, pulse duration  $\tau_p = 100 \mu s$  and at a repetition rate  $f_{rep} = 10$  Hz). As expected, thermometric signals are very weak: the measured peak values are in the range 1-100  $\mu V$  for a sensing current of 20  $\mu A$ . It should be stressed that thermometric signals are still perturbed (e.g. cross talk) by the heater signal even with careful electromagnetic shielding.

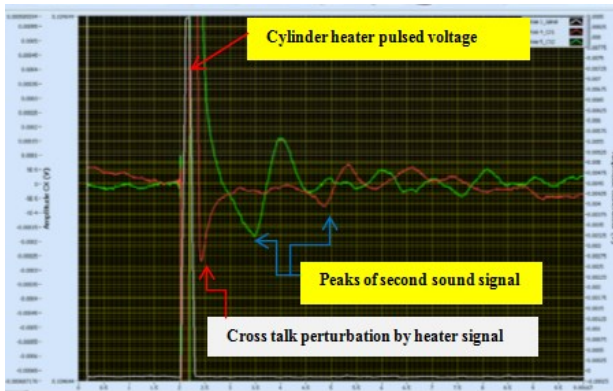


Fig. 11: Response signals of CERNOX #1 (red) and CERNOX #2 (green) to a pulsed heat flux  $Q_p = 38$  W.

The observed first peaks of the thermometric signals shown in Fig. 11 corresponds to heating  $\Delta T = 0.3$  mK for CX#2 and  $\Delta T = 0.08$  mK for CX#1. Moreover, the measured second velocity at  $T_{bath} = 2.1$  K as deduced from thermometric signals of Fig. 11 is 12.6 m/s which is close (to within 1.4 %) to precise measurements (e.g. 12.42 m/s) performed by Wang et al. [10]. The observed second sound signals shape and time structure, as measured either by OST or LRETIRETH, depends strongly on the experimental configuration and in particular on the heater geometry. More precisely, the geometry of the heat source or the excitation source that generates the second sound determines if the resulting wave is planar, cylindrical or spherical. The type of involved second sound wave determines in turns the temporal structure of the sensors response to a pulsed excitation. More precisely according to theory, in the case of cylindrical or spherical second sound wave configuration, the propagating shock wave should show a heating (compression) followed by cooling (rarefaction) at given location from the pulsed heat source.

Such behaviour was previously observed by several authors. In our case, for cylindrical heat source, one observes pseudo-sinusoidal response to a pulsed excitation as it is clearly shown in Fig 11-Fig. 12. The time structure of the observed OST or CX sensors signals are similar to damped oscillations, which led to misinterpretation by some previous studies. In the case of spherical second sound shock wave propagation (e.g. flat SMD heater), we observed (Fig. 13) the theoretically expected signal but with a slightly different time structure as compared to cylindrical case: the decay time of oscillations is shorter in the case of spherical wave.

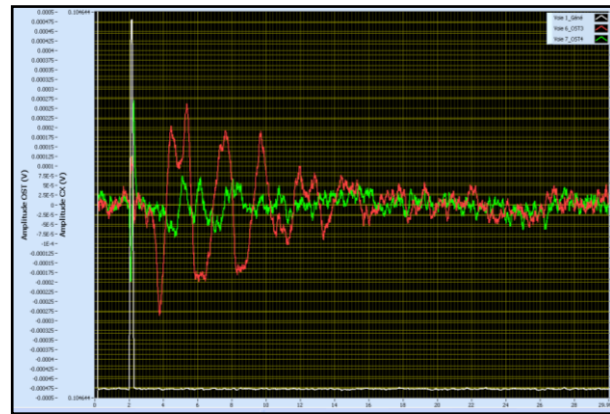


Fig. 12: Response of OST #3 (red) and OST #4 (green), at  $T_{bath} = 2.1$  K to a pulsed heat flux  $q_p = 48.3$  W/cm<sup>2</sup>, with  $\tau_p = 100 \mu s$  for  $V_p = 150$  V-Test cell#2: cylindrical heater area = 79.5 mm<sup>2</sup> (O.D = 5.3 mm, Length = 15 mm).



Fig. 13: Response of OST #1 (red) and OST #2 (green), at  $T_{bath} = 2.1$  K to a pulsed heat flux  $q_p = 753$  W/cm<sup>2</sup>, with  $\tau_p = 100 \mu s$  for  $V_p = 150$  V-Test cell#3: Flat SMD heater area = 5.1 mm<sup>2</sup>.

Additional tests will be carried out to clarify this behaviour and whether or not this is due to heat source geometry.

### Second Velocity

As mentioned above, second sound signals were successfully recorded by both OST and CX thermometers. From these data, we have deduced by cross-correlation experimental values of the second sound velocity  $U_2$ . The corresponding results, as deduced from OST signals, are illustrated in Fig. 14. Measurements were performed by two different procedure stabilize He II bath temperature at different values then subject the heaters to pulsed heat flux and simultaneously monitoring OST and CX signals versus time, b) subjecting the heaters to pulsed heat flux and simultaneously monitoring OST and CX signals versus time while He II bath temperature is slowly drifting. The data obtained by the two methods are in very good agreement. The solid red circles were obtained by the first method using the test cell#3 and cross correlation between OST#1 and OST#2. The solid blue triangles were obtained by the second method using

the test cell#2 and the time flight between heater and OST#3.

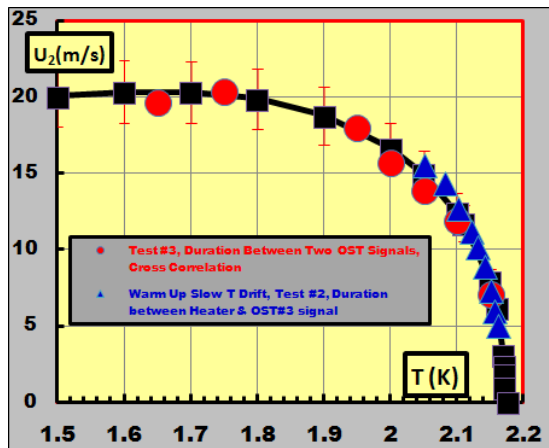


Fig. 14: Comparison of measured second sound velocity to previous experimental data (solid black line).

Moreover our experimental data are in very good agreement with previous experimental results reported by Donnelly group [10]. Note that second sound velocity was also deduced from the thermometric signals (e.g. time flight between heater and CERNOX #2) leading to data (not illustrated in Fig. 14) in very good agreement with those from OST sensors.

### Experimental Observations About Signal Time Structure

The pseudo-sinusoidal like response to a pulsed excitation shown in Fig. 12, was systematically studied as function of  $T_{\text{bath}}$ . This test was performed with test cell #2. The frequency of oscillations of OST#3 sensor was measured as function of second sound velocity (Fig. 15), which varies with  $T_{\text{bath}}$ . The peak heater power and pulse duration are respectively  $Q_p=38$  W and  $\tau_p=100$   $\mu$ s at a repetition rate  $f_{\text{rep}}=10$  Hz.

The results shown in Fig. 15 show a linear increase of the oscillation frequency with respect to second sound velocity. This confirms that these pseudo-oscillations have a physical meaning to be clarified and is not a characteristic of the OST membrane mechanical behaviour.

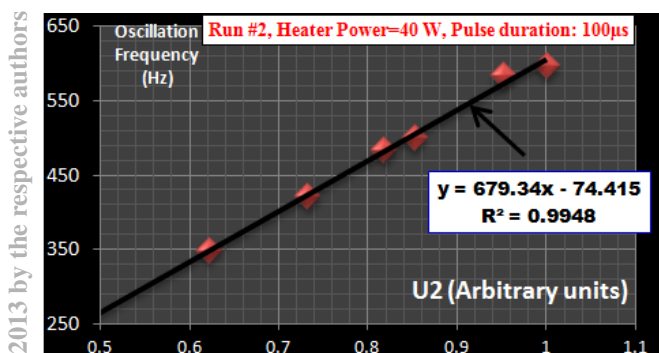


Fig. 15: Oscillation frequency versus second sound velocity.

## CONCLUSION AND OUTLOOK

In the frame of a R&D program dedicated to the development of diagnostic tools for in situ quench detection and locating in SRF Cavities, IPN developed its first prototypes of OST quench detectors and a cryogenic test stand for their calibration and full characterization in the saturated He II temperature range  $T_{\text{bath}}=1.6$  K-2.2 K. This device allows precise and controlled experimental simulation of SRF cavity quench using pulsed heat sources. This experimental set-up will help to progress in locating and characterizing quench sources in SRF cavities. Experimental tests on various bulk niobium SRF cavities (e.g. QWR, spoke and elliptical resonators) with quench detectors (OST and LRETIRETH) are planned in the near future. In particular, we plan to study the quench dynamics and critical size of hot spot normal resistive area leading to SRF cavity quench.

## ACKNOWLEDGMENT

Many thanks to the technical staff of Accelerators Division and Instrumentation Division of IPN Orsay for their valuable help in the various steps of preparation of all the tests.

## REFERENCES

- [1] Y. Yamamoto et al., NIM A729 (2013) 589.
- [2] Y. Yamamoto, E. Kako, T. Shishido, "Quench field and Location in Vertical Tests at KEK-STF", TUP116, these proceedings.
- [3] R. Brizzi, M. Fouaidy, T. Junquera, M.X. François "Thermometry of niobium surfaces in superfluid helium: a powerful diagnostic technique for superconducting RF cavities", HTD-Vol. 134, pp. 15-22, 1990.
- [4] M. Fouaidy et al., "Surface temperature measurements on superconducting cavities in superfluid helium" Proc. of the 5<sup>th</sup> Workshop on RF Superconductivity, Desy (Hamburg), August 91, Vol. 2, pp 547 – 576.
- [5] Q.S. Shu et al., Proc. of the 7<sup>th</sup> Workshop on RF Superconductivity, Gif-Sur-Yvette (France), pp. 431-435, 1995.
- [6] M. Fouaidy et al, "Analysis of effects in TESLA SRF cavities using surface scanning thermometers", Proc. of EPAC96, Barcelona, June 96.
- [7] M. Fouaidy, T. Junquera, "Heat transfer characteristics from a plane surface to a saturated He II bath", Cryogenics Vol. 37, N° 11, pp. 753-765, 1997.
- [8] R. A. Sherlock and D. O. Edwards, "Oscillating Super leak Second Sound Transducers", The Review of Scientific Instruments Vol. 41, 11 (1970) 1603.
- [9] Z.A. Conway et al., TTC report #2008-06.
- [10] R. T. Wang, W.T. Wagner, R. J. Donnelly, "Precision Second-Sound Velocity Measurements in Helium II", J. L.T.P, Vol. 68, Nos.5/6 (1987) 409.